

Supplementary Information

Flexible thermoelectrics: from silver chalcogenides to full-inorganic devices

Jiasheng Liang^{a,b,†}, Tuo Wang^{a,b,†}, Pengfei Qiu^a, Shiqi Yang^{a,b}, Chen Ming^a, Hongyi Chen^{a,b}, Qingfeng Song^{a,b}, Kunpeng Zhao^a, Tian-ran Wei^a, Dudi Ren^a, Yi-Yang Sun^a, Xun Shi^{a,c*}, Jian He^d, Lidong Chen^{a*}

^aState Key Laboratory of High Performance Ceramics and Superfine Microstructure, Shanghai Institute of Ceramics, Chinese Academy of Sciences, Shanghai 200050, China.

^bUniversity of Chinese Academy of Sciences, Beijing 100049, China.

^cState Key Laboratory of Metal Matrix Composites, School of Materials Science and Engineering, Shanghai Jiao Tong University, Shanghai, 200240, China

^dDepartment of Physics and Astronomy, Clemson University, Clemson, SC, 29634, USA

† These authors contributed equally to this work.

E-mail: xshi@mail.sic.ac.cn (X.S.); cld@mail.sic.ac.cn (L.C.)

Normalized maximum power density

As the heat released by the human body is given at “free” cost and unlimited, the power output is more relevant than the conversion efficiency for a wearable device. When the resistance of external electrical load is equal to the internal resistance (R_{in}) of TE module (device), the power output reaches the maximum value

(P_{max}),¹

$$P_{max} = \frac{(\alpha_p - \alpha_n)^2 \Delta T^2}{4R_{in}}, \quad (S1)$$

where ΔT is the temperature difference across the device, and α_n and α_p are the Seebeck coefficients of n -type and p -type legs, respectively. Eq. S1 can be rewritten as

$$P_{max} = \frac{(\alpha_p - \alpha_n)^2 \Delta T^2}{4\left(\frac{L}{\sigma_n A_n} + \frac{L}{\sigma_p A_p}\right)}, \quad (S2)$$

where σ_n and σ_p are the electrical conductivities of n -type and p -type legs, respectively; L is the length and A is the cross-sectional area of the leg. Assuming $A = A_n + A_p$ and $A_n/A_p = \varepsilon$, the normalized maximum power density ($P_{max}L/A$) is rewritten as

$$P_{max}L/A = \frac{(\alpha_p - \alpha_n)^2 \Delta T^2}{4(1 + \varepsilon)\left(\frac{1}{\sigma_n \varepsilon} + \frac{1}{\sigma_p}\right)}. \quad (S3)$$

As shown, the normalized maximum power density is governed by the electrical properties of the material of which the leg is made, the parameter ε , and ΔT . In our

six-couple in-plane $\text{Ag}_2\text{S}_{0.5}\text{Se}_{0.5}/\text{Pt-Rh}$ TE device, the contribution of Pt-Rh wire to ($P_{max}L/A$) is negligible because of its large electrical conductivity and low Seebeck coefficient.

Phase analysis of Ag_2S -based materials

The X-ray powder diffraction patterns of a series of $\text{Ag}_2(\text{S,Se})$, $\text{Ag}_2\text{S}_{0.8}\text{Te}_{0.2}$, and $\text{Ag}_2\text{S}_{0.5}\text{Se}_{0.45}\text{Te}_{0.05}$ samples are shown in Fig. S2a. A systematic peak shift to lower angles with increasing doping ratio was observed (cf. Fig. S2b). No discernible secondary phases were detected. The results of elemental mapping showed that Ag, S, and Se are homogeneous throughout the $\text{Ag}_2(\text{S, Se})$ samples (cf. Figs. S2c). No elemental agglomerations or secondary phases were detected. Similar phenomena were observed for $\text{Ag}_2(\text{S, Te})$ and $\text{Ag}_2(\text{S, Se, Te})$. Apparently, all Se and Te atoms have entered into the lattice of Ag_2S .

Calculations of shear and bulk modulus

The room temperature shear modulus (G_T) and bulk modulus (B_T) for $\text{Ag}_2(\text{S, Se})$ and $\text{Ag}_2(\text{S, Te})$ were derived from the measured transverse (v_t) and longitudinal (v_l) sound speed using the following formulas:

$$v_t = \sqrt{\frac{G_T}{d}} \quad (\text{S4})$$

and

$$v_l = \sqrt{\frac{B_T + \frac{4}{3}G_T}{d}}, \quad (\text{S5})$$

where d is the mass density.

The Poisson ratio is given by

$$\nu = \frac{2v_t^2 - v_l^2}{2(v_t^2 + v_l^2)}, \quad (S6)$$

Calculations of lattice thermal conductivity

The total thermal conductivity (κ) of a solid is composed of the carrier thermal conductivity (κ_c) and the lattice thermal conductivity (κ_L). The κ_c is estimated using the Wiedeman-Franz law ($\kappa_c = LT\sigma$, where L is the Lorenz number). According to the empirical equation $L = [1.5 + e^{\frac{-|\alpha|}{116}}] \times 10^8$ proposed by Kim *et al.*², the L values for $\text{Ag}_2\text{S}_{1-x}\text{Se}_x$ ($x = 0, 0.03, 0.1, 0.3, \text{ and } 0.5$) and $\text{Ag}_2\text{S}_{0.8}\text{Te}_{0.2}$ were calculated with the data shown in Fig. S3b. Based on the L values and measured σ values, the κ_L values for these materials were calculated by subtracting κ_c from the total κ . The temperature dependence of κ_L for all samples are shown in Fig. S3.

The Callaway model

In the Callaway model, the lattice thermal conductivity of a solid solution is given by³

$$\kappa_L = k_B / [4\pi v_s (ACT)^{1/2}] \tan^{-1} \left[\frac{K\theta}{\hbar} \cdot \left(\frac{A}{CT} \right)^{1/2} \right], \quad (S7)$$

where CT is the relaxation time for phonon-phonon scattering (C is a constant and T is the temperature), v_s is the mean sound speed, k_B is the Boltzman constant and A is the coefficient for the Rayleigh-type point defect scattering rate. In the phase pure Ag_2S ,

$$\kappa_{pure} = k_B^2 \Theta_D / [2\pi^2 v_s \hbar C T] \quad , (S8)$$

where Θ_D is the Debye temperature with a value of 108 K as calculated from the measured sound speed. The $A = \Omega_0 \Gamma / (4\pi v_s^3)$, where Ω_0 is the unit cell volume and Γ is the scattering parameter. The scattering parameter Γ has two contributions, Γ_M and Γ_S , where Γ_M and Γ_S are scattering parameters related to mass fluctuation and strain field fluctuation, respectively. They can be further expressed as

$$\Gamma = \Gamma_M + \Gamma_S = x(1-x) \left[\left(\frac{\Delta M}{M} \right)^2 + \varepsilon \left(\frac{\Delta a}{a} \right)^2 \right] \quad , (S9)$$

where ΔM and Δa are the difference in mass and lattice constants between S and Se atoms, and M and a are the molar mass and lattice constant of $\text{Ag}_2(\text{S}, \text{Se})$, respectively. The parameter ε is obtained by fitting experimental data.

Formation energy of defects

The first-principle calculations were performed based on the density functional theory (DFT) as implemented in VASP program⁴. The PBEsol functional⁵ was used to optimize the atomic structures and calculate the defect formation energy. Projector augmented wave (PAW)⁶ potentials were used to describe the core–valence interaction and plane-waves up to the kinetic energy of 272 eV were used as the basis set. A (3×2×2) 144-atom supercell was used to model the defects. A 2×2×2 k -point mesh was used to sample the Brillouin zone of the supercell. The atomic structures were relaxed until the residual forces on all atoms were smaller than 0.01 eV.

The formation energy of a lattice defect (D) in a charge state q was calculated

according to

$$E_{form}(D^q) = E(D^q) - E_{bulk} + \sum_i \Delta n_i \mu_i + q(E_F + E_{VBM}) \quad , (S9)$$

Where $E(D^q)$ and E_{bulk} are the total energies of defect-containing and defect-free supercells, respectively, Δn_i is the quantity of the i -th species exchanged in forming the defect and μ_i is the chemical potential of the i -th species. The Fermi level (E_F) is referenced to the valence band maximum (VBM) energy (E_{VBM}) of the defect-free supercell. μ_s and μ_{Ag} were referenced to the bulk sulfur in the orthorhombic α -phase with a space group $Cmcm$ and bulk silver in its fcc structure, respectively. The transition level of a defect from a charge neutral state to q charge state, $\varepsilon(0/q)$, was calculated as

$$\varepsilon(0/q) = \frac{1}{q} (E(D^0) - E(D^q)) - E_{VBM} \quad , (S10)$$

We considered two most probable native donor defects, *i.e.*, sulfur vacancy (V_S) and silver interstitial (Ag_i). The calculated E_{form} of V_S and Ag_i in neutral charge state are 0.56 and 0.91 eV, respectively. We found that V_S is neither a donor nor an acceptor because its donor levels are so deep that they appear below the VBM, and similarly its acceptor levels are above the conduction band minimum (CBM). In contrast, Ag_i was found to be a shallow donor with a $\varepsilon(0/+)$ transition level 0.15 eV above the CBM. It is expected that increasing the supercell size will reduce the image-charge interactions in the calculations of the charged states, thereby making the transition level closer to the CBM⁷. It is plausible to argue that the Ag_i lattice

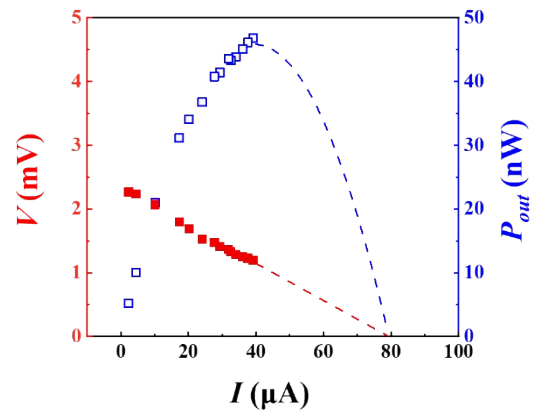
defects account for the native charge carriers observed in experiments. The optimized atomic structure including Ag_i is shown in Figs. S8a and S8b, where the Ag_i atom lies at the center of an S-Ag eight-member ring, and one Ag atom is pushed out of the ring with respect to its original position.

To examine the effect of Se doping on the formation energy of Ag_i , we replaced the neighboring S atoms around the Ag_i atom by Se atoms gradually. The formation energy was calculated by taking the energy difference between the results with and without the Ag_i atom, where both structures were re-optimized. As shown in Fig. S8c, the E_{form} of Ag_i in monoclinic Ag_2S is 0.91 eV. With increasing Se content, E_{form} gradually decreases. When six neighboring S atoms are replaced by Se atoms, the E_{form} of Ag_i decreases to 0.72 eV. This result indicates that increasing Se concentration in $Ag_2S_1Se_{1-x}$ tends to facilitate more Ag_i defects and thus higher electron concentration, which agrees with the experimental observations.

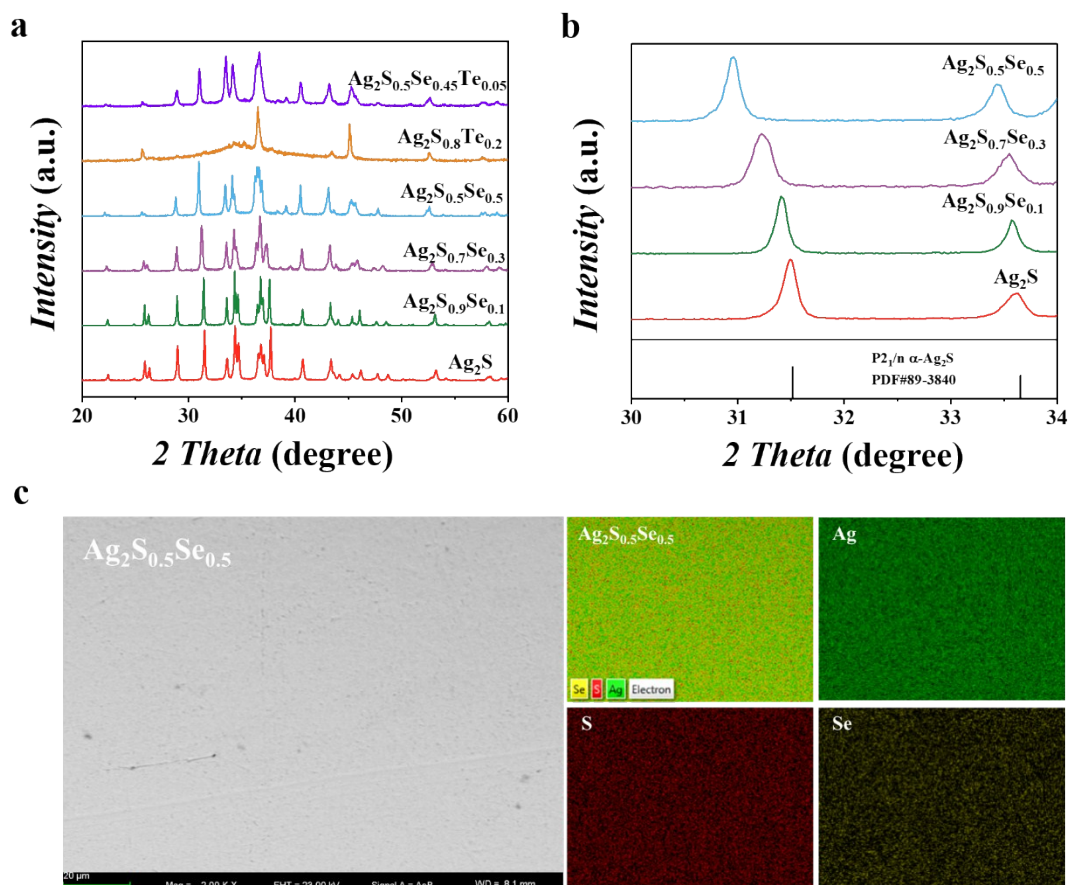
Electron band structure calculations

The band structure calculation was performed using the same method as that in the formation energy calculations above. For $Ag_2S_{0.5}Se_{0.5}$ solid solution, we considered an ordered structure by replacing two of the four S atoms with Se atoms in the optimized unit cell of Ag_2S which consists of 16 atoms. Then the volume of the ordered structure was relaxed by keeping the ions and the shape of the cell fixed. A $16 \times 8 \times 8$ k -point mesh was used to calculate the charge density. The effective masses were calculated by fitting the electronic band structure to quadratic functions near the VBM and CBM (both are at Γ point) along the three principal axes, and the results

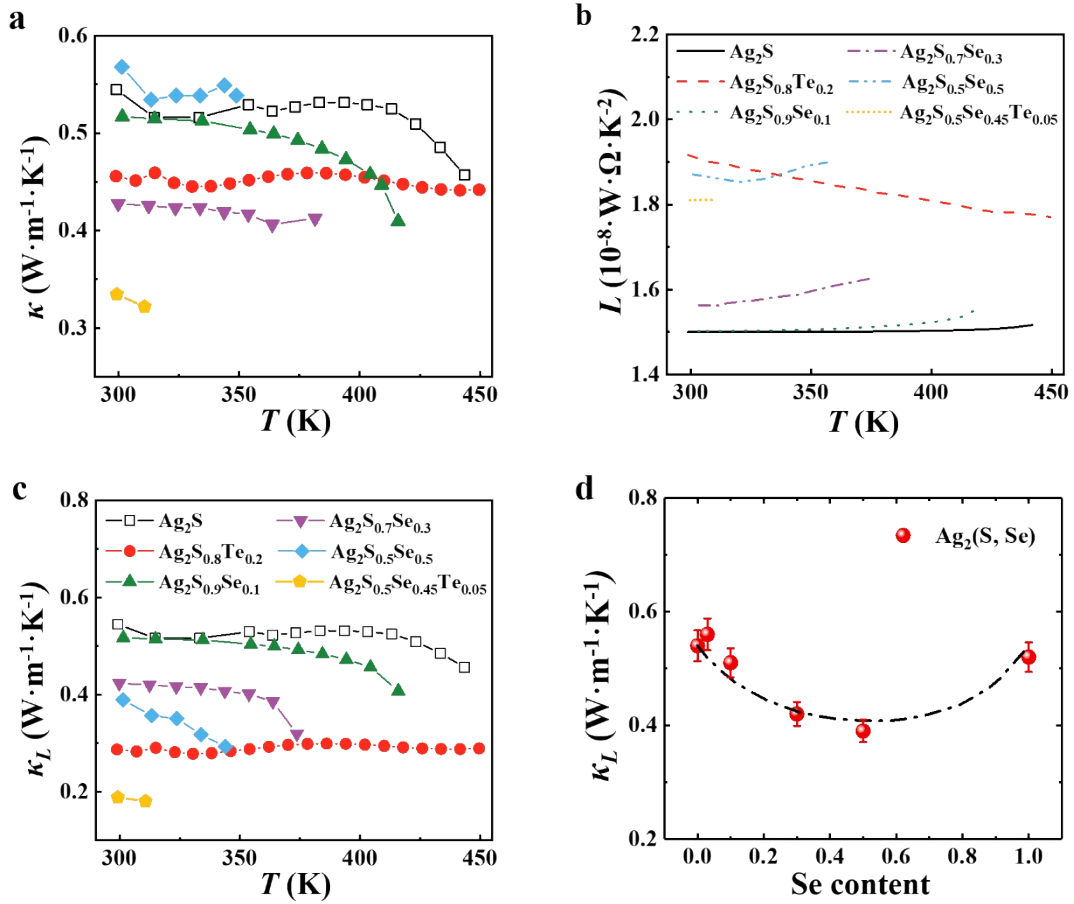
are listed in Table SII.

a**b**

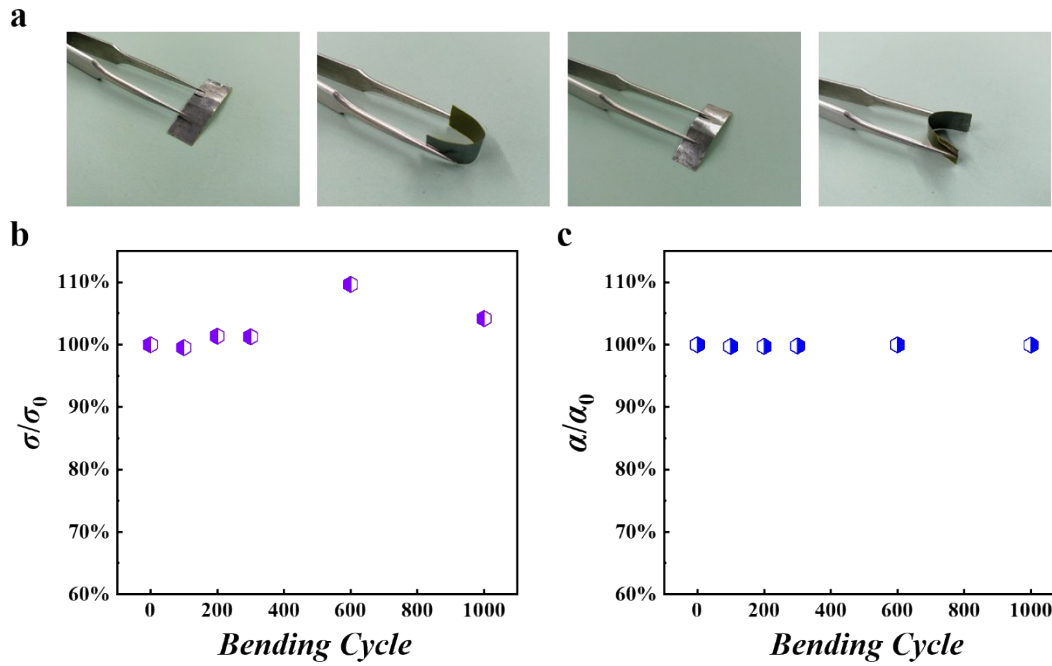
Supplementary Figure 1 | An $\text{Ag}_2(\text{S, Se})$ -based wearable device used for harvesting body heat. a) Optical image of the $\text{Ag}_2\text{S}_{0.5}\text{Se}_{0.5}/\text{Pt-Rh}$ wearable device with a tilted architecture, **b)** Open circuit voltage V and power output P_{out} as a function of current I for the $\text{Ag}_2\text{S}_{0.5}\text{Se}_{0.5}/\text{Pt-Rh}$ wearable device under an ambient temperature about 290K.



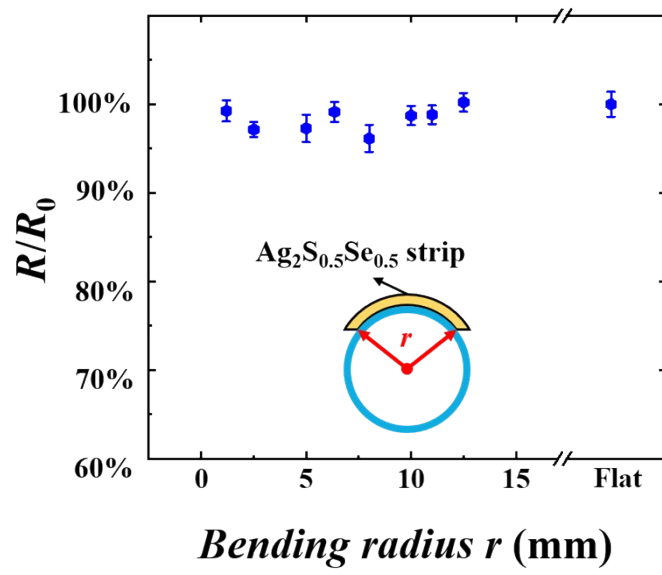
Supplementary Figure 2 | Phase compositions of Ag₂S-based materials. a) Powder X-ray diffraction patterns for Ag₂(S, Se), Ag₂(S, Te), and Ag₂(S, Se, Te) at room temperature. b) Magnification of the X-ray diffraction patterns at 2 θ of 30-34° for Ag₂S_{1-x}Se_x (x = 0, 0.1, 0.3, and 0.5). c) Backscatter electron (AsB) image and elemental energy dispersive spectroscopy (EDS) mappings of Ag₂S_{0.5}Se_{0.5} at 2000 \times magnification.



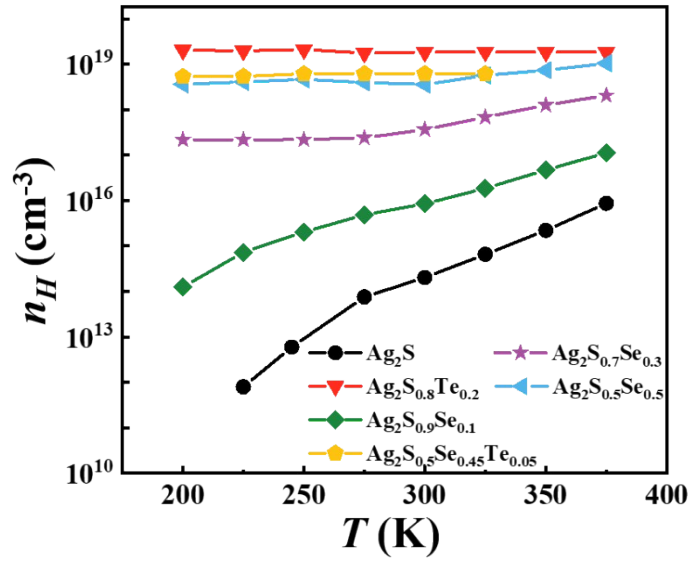
Supplementary Figure 3 | Thermal transport properties of Ag₂S-based materials. Temperature dependences of **a**) total thermal conductivity κ , **b**) Lorenz number L , and **c**) lattice thermal conductivity κ_L for Ag₂S_{1-x}Se_x ($x = 0, 0.1, 0.3$, and 0.5), Ag₂S_{0.8}Te_{0.2}, and Ag₂S_{0.5}Se_{0.45}Te_{0.05}. **d**) Lattice thermal conductivity κ_L as a function of Se content at 300 K. The filled circles are experimental data. The data of Ag₂Se are taken from Ref.8. The dash dot line is the results calculated by the Callaway model.



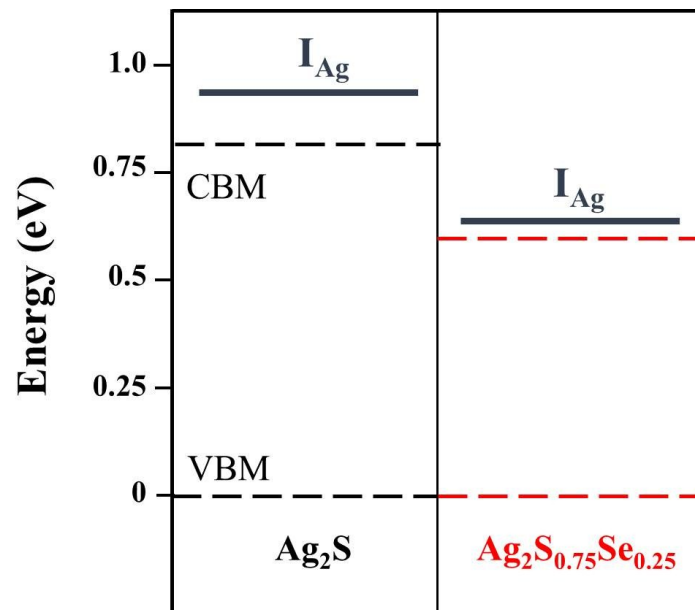
Supplementary Figure 4 | Robustness of Ag₂S-based materials. **a)** Optical images of the Ag₂S_{0.5}Se_{0.5} foil used for bending test. The bending angle is around 120 degree. The foil is firstly bent in one direction and then restored to its initial shape, followed by bending in the opposite direction. **b)** Relative electrical conductivity variation σ/σ_0 and **c)** relative Seebeck coefficient variation α/α_0 of the Ag₂S_{0.5}Se_{0.5} foil after various number of times of bending cycles.



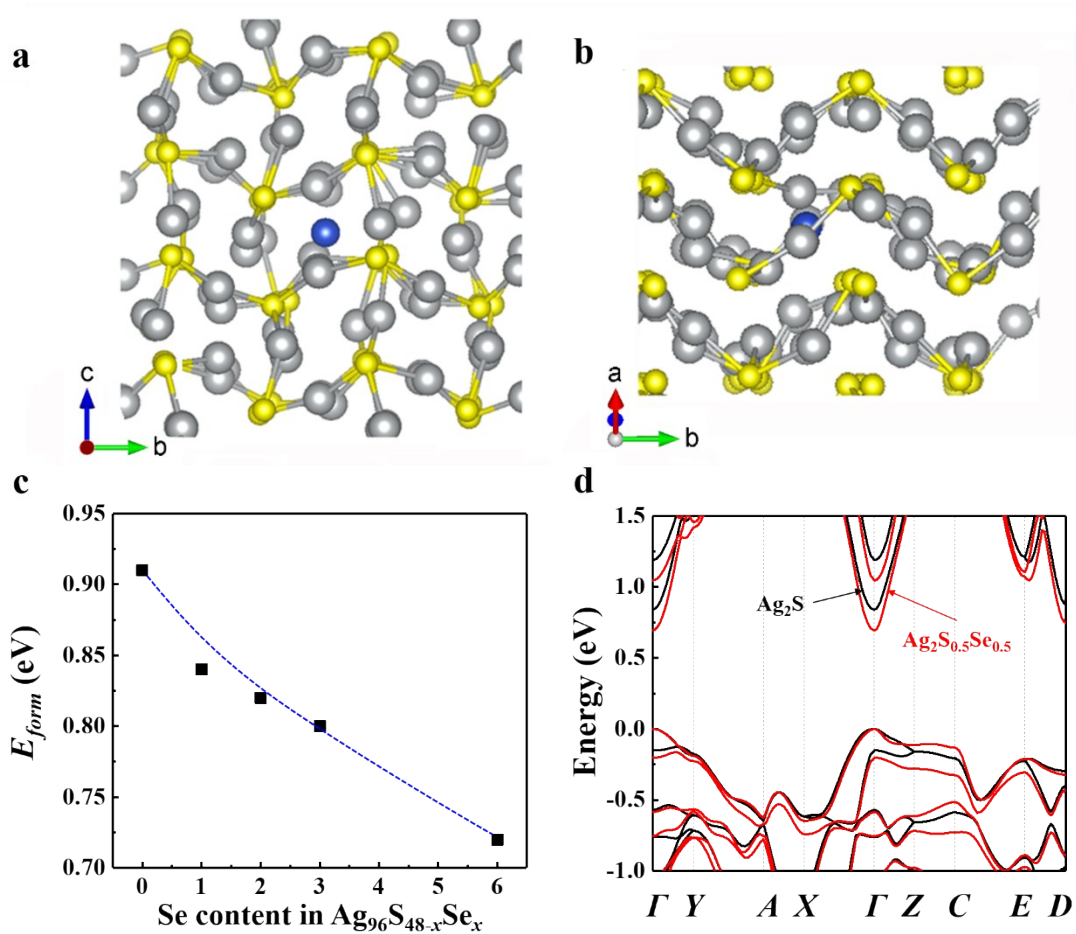
Supplementary Figure 5 | stability of $\text{Ag}_2\text{S}_{0.5}\text{Se}_{0.5}$ stripe under strain. Relative variation of resistance of a $\text{Ag}_2\text{S}_{0.5}\text{Se}_{0.5}$ slice under different bending radii r .



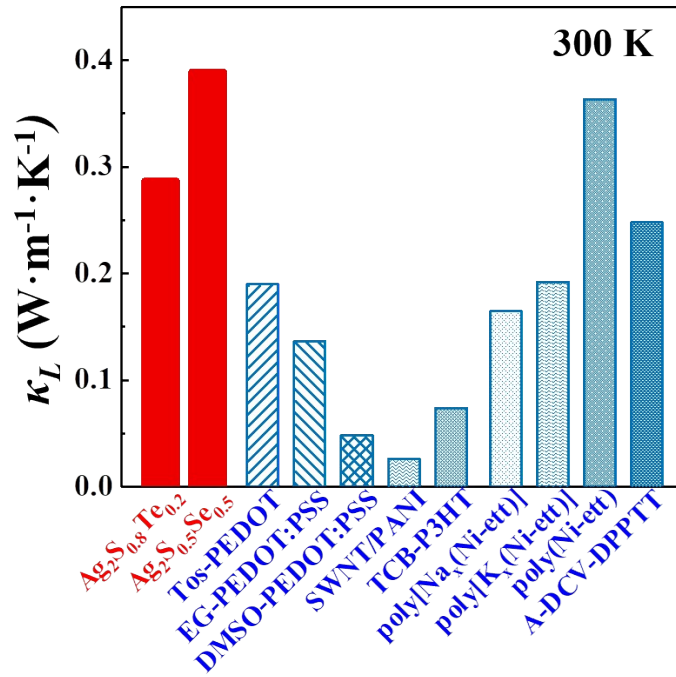
Supplementary Figure 6 | Carrier concentrations of Ag₂S-based materials. Temperature dependence of carrier concentration n_H for Ag₂S_{1-x}Se_x ($x = 0, 0.1, 0.3,$ and 0.5), Ag₂S_{0.8}Te_{0.2}, and Ag₂S_{0.5}Se_{0.45}Te_{0.05}.



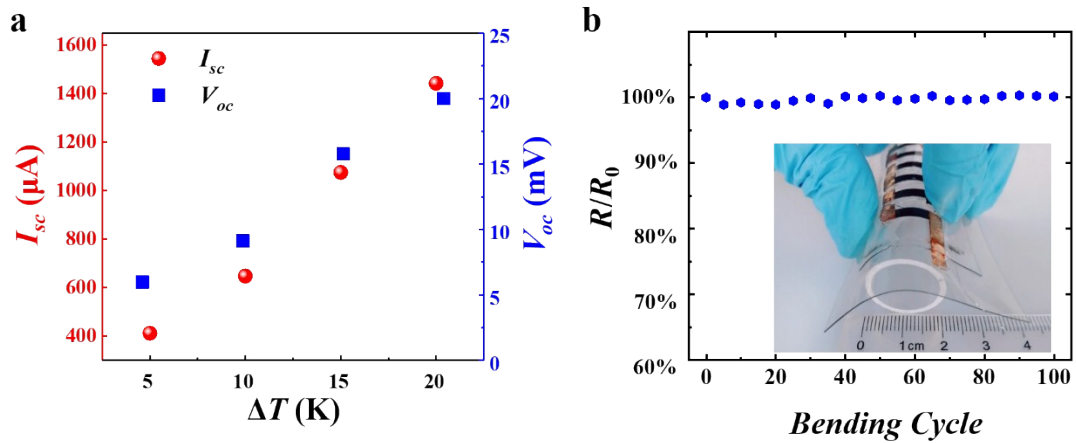
Supplementary Figure 7 | Calculated defect activation energy (E_a) values for pure Ag₂S and Ag₂(S,Se).



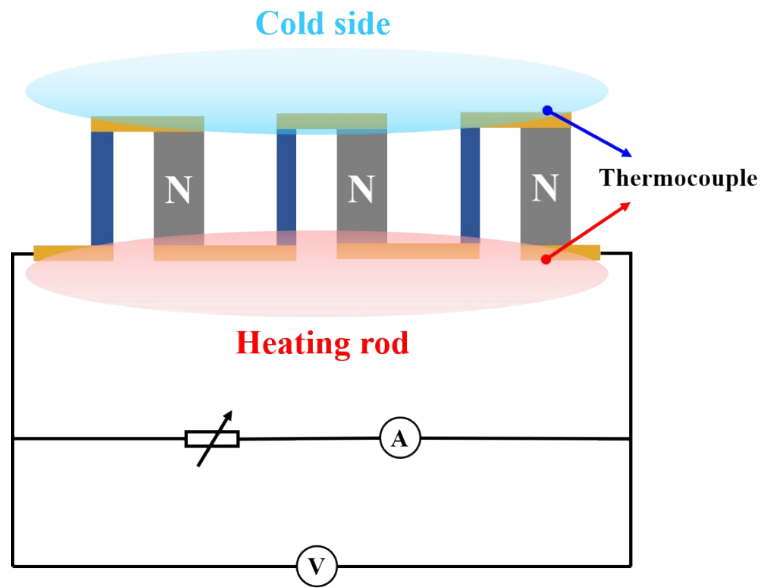
Supplementary Figure 8 | Formation energy of the interstitial silver defect and band structure of Ag_2S -based compounds. **a)** Top view and **b)** side view of the atomic structure of interstitial silver defect in monoclinic Ag_2S phase. The yellow, grey, and blue balls represent sulfur, silver, and silver interstitial atoms, respectively. **c)** Formation energy E_{form} of the interstitial silver defect calculated for a supercell of $Ag_{96}S_{48-x}Se_x$ with varying Se concentration. The dashed line is guided to the eyes. **d)** Calculated band structures for Ag_2S and $Ag_2S_{0.5}Se_{0.5}$.



Supplementary Figure 9| Comparison of room temperature lattice thermal conductivity κ_L between Ag₂S-based inorganic materials and some representative organic TE materials. The room temperature κ_L data⁹⁻¹⁶ are obtained by subtracting the carrier thermal conductivity κ_c from the measured total thermal conductivity κ . The κ_c is estimated according to the Wiedemann-Franz relation with a Lorenz number $L = 2.0 \times 10^{-8} \cdot \text{W} \cdot \Omega \cdot \text{K}^{-2}$.



Supplementary Figure 10 | Performance and stability of $Ag_2S_{0.5}Se_{0.5}/Pt-Rh$ TE device. Short circuit I_{sc} and open circuit voltage V_{oc} for the $Ag_2S_{0.5}Se_{0.5}/Pt-Rh$ TE device at different temperature difference ΔT . **b)** Relative electrical resistance variation R/R_0 of the $Ag_2S_{0.5}Se_{0.5}/Pt-Rh$ TE device after bending various number of times. The inset shows the optical image for the bended device. The bending radius is 10 mm. After each bending, the device is restored to its initial shape for the follow-up resistance measurement and the next bending-measurement cycle.



Supplementary Figure 11 | Device characterization details. Schematic of the self-setup power density measurement system.

Supplementary Table I. Phase-transition temperature(T_c), Hall carrier concentration (n_H), carrier mobility (μ_H), electrical conductivity (σ), Seebeck coefficient (S), power factor (PF), TE figure of merit(zT), thermal conductivity (κ); transverse (v_t), longitudinal (v_l), and averaged (v_{avg}) sound speed; shear modulus (G_T), bulk modulus (B_T), the (B_T/G_T) ratio, Poisson's ratio (ν), and lattice thermal conductivity (κ_L) of $Ag_2(S, Se)$, $Ag_2(S, Te)$, and $Ag_2(S, Se, Te)$. These are all room temperature values unless otherwise noted.

Compositions	Ag_2S	$Ag_2S_{0.9}Se_{0.1}$	$Ag_2S_{0.7}Se_{0.3}$	$Ag_2S_{0.5}Se_{0.5}$	$Ag_2S_{0.8}Te_{0.2}$	$Ag_2S_{0.5}Se_{0.45}Te_{0.05}$
T_c (K)	449	420	382	355	\	330
n_H (cm^{-3})	1.6×10^{14}	8.5×10^{15}	3.6×10^{17}	3.6×10^{18}	1.9×10^{19}	6.2×10^{18}
μ_H ($cm^2 \cdot V^{-1} \cdot s^{-1}$)	39.8	19.6	182	520	135	272
σ ($S \cdot m^{-1}$)	0.102	2.67	1047	3.0×10^4	3.9×10^4	2.7×10^4
S ($\mu V \cdot K^{-1}$)	-1051	-714	-321	-123	-101	-136
PF ($\mu W \cdot cm^{-1} \cdot K^{-2}$)	0.0011	0.013	1.08	4.84	3.88	4.96
zT	6.3×10^{-5}	7.6×10^{-4}	0.075	0.26	0.25	0.44
κ ($W \cdot m^{-1} \cdot K^{-1}$)	0.54	0.52	0.43	0.57	0.46	0.33
κ_L ($W \cdot m^{-1} \cdot K^{-1}$)	0.54	0.52	0.42	0.39	0.29	0.19
v_t ($m \cdot s^{-1}$)	1128	1090	1047	1084	1041	1099
v_l ($m \cdot s^{-1}$)	2596	2510	2645	2886	2406	2807
v_{avg} ($m \cdot s^{-1}$)	1617	1563	1579	1685	1496	1688
G_T (GPa)	9.2	8.8	8.2	9.1	8.0	9.4
B_T (GPa)	36.5	34.8	41.7	52.1	32.1	48.9
B_T/G_T	3.97	3.95	5.09	5.73	4.01	5.20
ν	0.38	0.38	0.41	0.42	0.38	0.41

Supplementary Table II. Calculated electron effective masses of monoclinic Ag_2S and $\text{Ag}_2\text{S}_{0.5}\text{Se}_{0.5}$ based on the calculated band structure shown in Fig. S6d.

\square	Valence band (m_0)			Conduction band (m_0)		
Ag_2S	$\Gamma \rightarrow \text{Y}$	$\Gamma \rightarrow \text{E}$	$\Gamma \rightarrow \text{X}$	$\Gamma \rightarrow \text{Y}$	$\Gamma \rightarrow \text{E}$	$\Gamma \rightarrow \text{X}$
	1.95	2.54	0.90	0.46	0.47	0.27
\square	Valence band (m_0)			Conduction band (m_0)		
$\text{Ag}_2\text{S}_{0.5}\text{Se}_{0.5}$	$\Gamma \rightarrow \text{Y}$	$\Gamma \rightarrow \text{E}$	$\Gamma \rightarrow \text{X}$	$\Gamma \rightarrow \text{Y}$	$\Gamma \rightarrow \text{E}$	$\Gamma \rightarrow \text{X}$
	1.05	2.01	0.53	0.37	0.43	0.21

References

1. Nolas, G.S., Sharp, J., Goldsmid, J. Thermoelectrics: basic principles and new materials developments, *Springer Science & Business Media* 2013.
2. Kim, H.-S., Gibbs, Z. M., Tang, Y., Wang, H. & Snyder, G. J. Characterization of Lorenz number with Seebeck coefficient measurement. *Appl. Phys. Lett. Mater.* **3**, 041506 (2015).
3. Callaway, J. Model for lattice thermal conductivity at low temperatures. *Phys. Rev.* **113**, 1046 (1959).
4. Kresse, G. & Furthmüller, J. Efficiency of ab-initio total energy calculations for metals and semiconductors using a plane-wave basis set. *Computational Materials Science* **6**, 15-50 (1996).
5. Perdew, J. P. *et al.* Restoring the density-gradient expansion for exchange in solids and surfaces. *Phys. Rev. Lett.* **100**, 136406 (2008).
6. Kresse, G. & Joubert, D. From ultrasoft pseudopotentials to the projector augmented-wave method. *Phys. Rev. B* **59**, 1758-1775 (1999).
7. Freysoldt, C., Neugebauer, J. & Van de Walle, C. G. Fully Ab Initio Finite-Size Corrections for Charged-Defect Supercell Calculations. *Phys. Rev. Lett.* **102**, 016402 (2009).
8. Ferhat, M. & Nagao, J. Thermoelectric and transport properties of β -Ag₂Se compounds. *J. Appl. Phys.* **88**, 813-816 (2000).
9. Bubnova, O. *et al.* Optimization of the thermoelectric figure of merit in the conducting polymer poly(3,4-ethylenedioxythiophene). *Nat. Mater.* **10**, 429-433 (2011).
10. Sun, Y. *et al.* Organic thermoelectric materials and devices based on p- and n-type poly(metal 1,1,2,2-ethenetetrathiolate)s. *Adv. Mater.* **24**, 932-937 (2012).
11. Kim, G. H., Shao, L., Zhang, K. & Pipe, K. P. Engineered doping of organic semiconductors for enhanced thermoelectric efficiency. *Nat. Mater.* **12**, 719-723 (2013).
12. Yao, Q., Wang, Q., Wang, L. & Chen, L. Abnormally enhanced thermoelectric transport properties of SWNT/PANI hybrid films by the strengthened PANI molecular ordering. *Energy Environ. Sci.* **7**, 3801-3807 (2014).
13. Qu, S. *et al.* Highly anisotropic P3HT films with enhanced thermoelectric performance via organic small molecule epitaxy. *NPG Asia Mater.* **8**, e292-e292 (2016).
14. Sun, Y. *et al.* Flexible n-Type High-Performance Thermoelectric Thin Films of Poly(nickel-ethylenetetrathiolate) Prepared by an Electrochemical Method. *Adv. Mater.* **28**, 3351-3358 (2016).
15. Huang, D. *et al.* Conjugated-Backbone Effect of Organic Small Molecules for n-Type Thermoelectric Materials with ZT over 0.2. *J. Am. Chem. Soc.* **139**, 13013-13023 (2017).
16. Wang, H., Yi, S.-i., Pu, X. & Yu, C. Simultaneously Improving Electrical Conductivity and Thermopower of Polyaniline Composites by Utilizing Carbon Nanotubes as High Mobility Conduits. *ACS Applied Materials & Interfaces* **7**, 9589-9597 (2015).